Available online at www.sciencedirect.com
SCIENCE DIRECT®
ELSEVIER
International Journal of Solids and Structures 42 (2005) 5036–5056
INTERNATIONAL JOURNAL OF SOLIDS and STRUCTURES
www.elsevier.com/locate/ijsolstr

A multi-scale simulation of tungsten film delamination from silicon substrate

Luming Shen, Zhen Chen *

Structural Group, Department of Civil and Environmental Engineering, University of Missouri-Columbia, Columbia, MO 65211-2200, USA

Received 15 August 2004; received in revised form 13 February 2005
Available online 28 March 2005

Abstract

To bridge the different spatial scales involved in the process of tungsten (W) film delaminating from silicon (Si) substrate, a multi-scale simulation procedure is proposed via a sequential approach. In the proposed procedure, a bifurcation-based decohesion model, which represents the link between molecular and continuum scales, is first formulated within the framework of continuum mechanics. Molecular dynamics (MD) simulation of a single crystal W block under tension is conducted to investigate the effect of specimen size and loading rate on the material properties. The proposed decohesion model is then calibrated by using MD simulation of a single crystal W block under tension and using available experimental data, with a power scaling law to account for the size effect. A multi-scale model-based simulation of W film delamination from Si substrate is performed by using the proposed procedure within the framework of the material point method. The simulated results provide new insights into the mechanisms of the film delamination process.

Keywords: Multi-scale simulation; Film delamination; Molecular dynamics; Size effect

1. Introduction

Thin films usually develop high residual stresses during the deposition process. The films subjected to large residual stresses may fail by delaminating and buckling away from the substrates in the working environment. The delamination of compressed films has been studied by many researchers in both academia and industry, as shown by representative papers (Gioia and Ortiz, 1997; Hutchinson and Suo, 1991;

* Corresponding author. Fax: +1 573 882 4784.
E-mail address: chenzh@missouri.edu (Z. Chen).

0020-7683/$ - see front matter © 2005 Elsevier Ltd. All rights reserved.
doi:10.1016/j.ijsolstr.2005.02.021

Wan and Mai, 1995). Existing approaches are mainly based on conventional elastic stability theory and interfacial fracture mechanics, with a focus on the stability of blisters (Audoly, 1999). Recently, much research has been conducted to model and simulate pattern formation during the delamination process, based on the buckling-driven mechanism (Crosby and Bradley, 1999; Huang and Suo, 2002; Moldovan and Golubovic, 1999; among others). However, a systematic study of the complete process from the formation of films to their eventual delamination from substrates is not yet available from the open literature, due to the complexity of multi-physics and multi-scales involved.

Based on the experimental observation of the transition from tensile to compressive stress as a function of the argon gas pressure in magnetron sputter-deposited tungsten (W) film onto silicon (Si) substrate (Shen et al., 2000), Chen et al. (in press) proposed that the delamination of compressed films is essentially due to the interaction between geometrical and material instabilities which results in the formation and evolution of localization, depending on different stress states in the domain of influence. By formulating a bifurcation-based decohesion model within the framework of the material point method (MPM), which is one of the "meshfree" methods (Chen et al., 2002), a numerical effort was made to investigate the transition from continuous to discontinuous failure modes involved in the W film delaminating from the Si substrate. Within the framework of continuum mechanics, the numerical study of the effects of aspect ratio and failure mode on the evolution of failure patterns under different boundary conditions provides a better understanding on the physics behind the film delamination process (Chen et al., in press).

However, the bifurcation-based simulation of the transition from localization to decohesion in the film delamination process is based on a phenomenological framework which could only provide a qualitative analysis of film delamination process. The bifurcation-based decohesion model, as proposed by Chen et al. (in press) is formulated via thermodynamics constraints with the result that the dissipation inequality is automatically satisfied. However, the constitutive relation of decohesion–traction, $\tau(\bar{u})$, as a key part of the decohesion model, cannot be calibrated via existing experimental techniques. Since the decohesion–traction constitutive relation is directly related to the interatomic binding energy and film microstructure developed during the film formation process, atomistic simulation might provide required information for establishing the decohesion model. Furthermore, the size of the film–substrate structure usually ranges from nano/micro to macroscale, and which is beyond the capability of the conventional continuum mechanics. Hence, a multi-scale decohesion–traction model is required to accommodate the suitable constitutive laws for the film structures at different size scales. In other words, a thorough understanding of the physics behind the film delamination process necessitates a multi-scale investigation ranging from atomistic simulation to continuum mechanics.

For the purpose of simplicity, a multi-scale sequential approach is proposed in this study, as illustrated in Fig. 1, to simulate the film delamination process. When bifurcation occurs in the MPM discretization of macroscopic responses, the proposed procedure would zoom in to the desired scale level in order to obtain the $\tau(\bar{u})$ constitutive relation curve. By coupling the multi-scale $\tau(\bar{u})$ constitutive law with the discontinuous bifurcation analysis within the framework of the MPM, the multi-degree discontinuous failure modes involved in the film delamination process could then be simulated.

With the rapid development of micro-electromechanical systems (MEMS) and nano-technology, atomistic simulation of mechanical behavior of metals has drawn considerable attention in recent years (Horstemeyer et al., 2001; Hu et al., 1998; Li and Yip, 2002; Liang and Zhou, 2003; Makarov et al., 2001; among others). The deformation of atomic system at finite temperatures in general is an intrinsically dynamic process. Size and strain rate effects arise out of several factors and play important roles in determining the response of nano-structures. The behavior and properties of micro/nano-structure are size-dependent due to the discreteness of atomic system, crystal arrangement and boundary condition. The dynamic inertia effect and the finite speeds at which lattice waves propagate also introduce the size effect to the problem and contribute to the size-dependence of atomic behavior. The inertia effect and finite wave speeds, along with

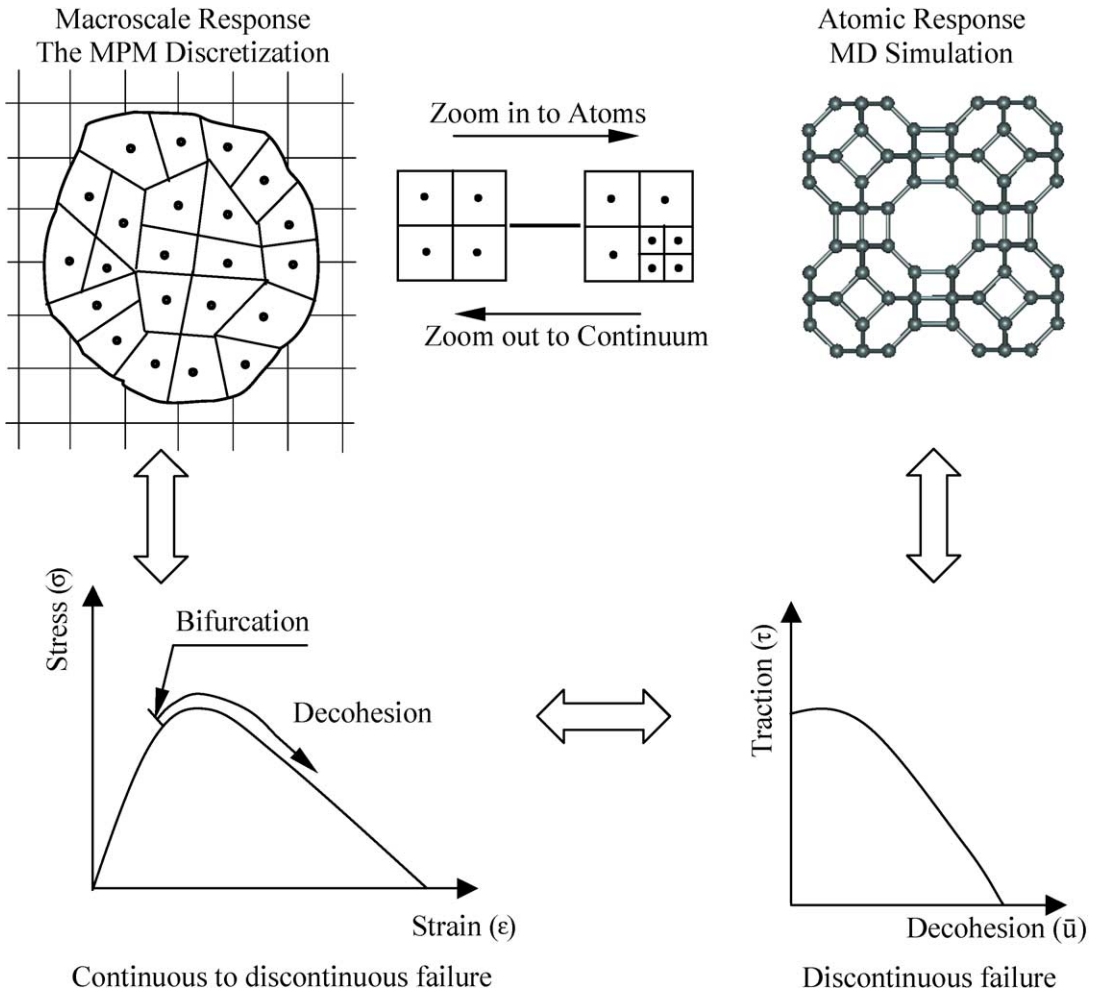

Fig. 1. Link between continuum mechanics and atomistic simulation.

phonon effects, also cause the response of nano-structures to be deformation-rate dependent. A part of this study thus focuses on the size and rate effects on the constitutive law of single crystal W block under tension in order to develop a multi-scale decohesion–traction model for W.

To determine material properties for elasto-plasticity and decohesion at different size scales, a power scaling law is proposed to account for the effect of structure size. Thus, MD simulation of single crystal W block under tension could be combined with available experimental data to develop a multi-scale $\tau(\bar{u})$ model for W based on the proposed scaling law. The multi-scale decohesion–traction model is then employed to simulate the film delamination process.

The remaining sections of the paper are arranged as follows. To be self-contained, a brief introduction of the bifurcation-based decohesion model within the framework of continuum mechanics is presented in Section 2. The MD simulation of single crystal W block under tensile loading is conducted in Section 3, which is followed by the formulation of the multi-scale decohesion–traction relation for W in Section 4. The multi-scale simulation of W film delamination from Si substrate is presented in Section 5. The conclusions are given in the last section.

2. Bifurcation-based decohesion model

To catch the essential feature of the film delamination process, a discrete constitutive model was formulated by Chen et al. (in press) by using the bifurcation analysis to predict decohesion or separation of continuum. As can be seen from Fig. 2, discontinuous bifurcation can occur before, at or after the peak state, depending on the continuum tangent stiffness tensor and stress state. It is therefore not rigorous to distribute arbitrarily cohesive surfaces in a computational mesh and initiate decohesion at the peak state in order to achieve computational efficiency, as discussed by the representative papers (Klein et al., 2000; Schreyer et al., 1999; Xu and Needleman, 1994). Based on a recent study (Chen and Fang, 2001), in fact, the discontinuous bifurcation analysis could be performed without too much computational cost if an associated von Mises elastoplasticity model is used with a linear hardening and softening law. Hence, the proposed discrete model is coupled with the bifurcation analysis based on the von Mises model (Chen et al., in press). As a result, rigorous and mesh-objective results could be obtained since the location and orientation of the cohesive surfaces are determined via the discontinuous bifurcation analysis (Shen and Chen, in press).

By taking the bifurcation point as the initiation of decohesion, the transition from continuous to discontinuous failure modes could be simulated. As shown in Fig. 3 for a plane strain problem, **n** and **t** represent the unit normal and tangent vectors to the cohesive surface whose orientation is obtained through bifurcation analysis. To determine the constitutive relation between traction $\boldsymbol{\tau}$ and decohesion (displacement jump) $\mathbf{u}^{\mathrm{d}}$, the following equations must be solved for a given total strain increment:

$$\mathrm{d}\boldsymbol{\sigma} = \mathbf{E}\colon(\mathrm{d}\boldsymbol{\varepsilon} - \mathrm{d}\boldsymbol{\varepsilon}^{\mathrm{d}}) \quad \text{Continuum elastoplasticity} \tag{1.1}$$

$$\boldsymbol{\tau} = \boldsymbol{\sigma}\cdot\mathbf{n} \quad \text{Traction equilibrium} \tag{1.2}$$

$$\mathrm{d}\mathbf{u}^{\mathrm{d}} = \mathrm{d}\lambda^{\mathrm{d}}\mathbf{m}^{\mathrm{e}} \quad \text{Evolution of decohesion} \tag{1.3}$$

$$\mathrm{d}\boldsymbol{\varepsilon}^{\mathrm{d}} = \frac{\mathrm{d}\lambda^{\mathrm{d}}}{2L_e}(\mathbf{n}\otimes\mathbf{m}^{\mathrm{e}} + \mathbf{m}^{\mathrm{e}}\otimes\mathbf{n}) \quad \text{Decohesion strain} \tag{1.4}$$

$$F^{\mathrm{d}} = \tau^{\mathrm{e}} - U_0[1 - (\Delta\lambda^{\mathrm{d}})^q] = 0 \quad \text{Consistency condition} \tag{1.5}$$

where **E** is linear elasticity tensor, λ^{d} is a dimensionless monotonically increasing variable characterizing the evolution of decohesion, namely, effective decohesion, L_{e} is the effective length representing the ratio of the

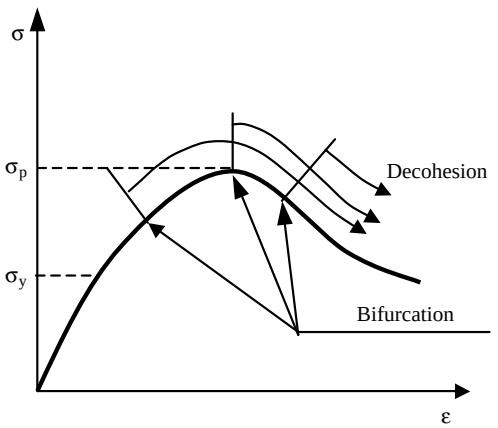

Fig. 2. Discontinuous bifurcation might occur before, at, or after the limit state.

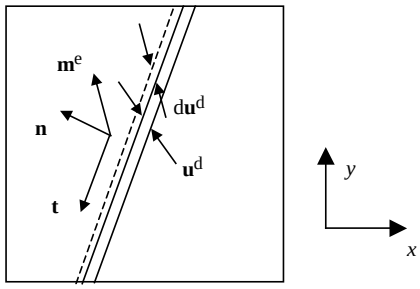

Fig. 3. A material element with decohesion in a plane strain problem.

volume to the area of the decohesion within a material element. It is assumed that no additional plastic strain would occur as long as decohesion evolves in the material element. For the purpose of simplicity, an associated evolution equation is employed, namely

$$\mathbf{m}^{\mathrm{e}} = \bar{u}_0 \frac{\mathbf{A}_{\mathrm{d}} \cdot \boldsymbol{\tau}}{(\boldsymbol{\tau} \cdot \mathbf{A}_{\mathrm{d}} \cdot \boldsymbol{\tau})^{\frac{1}{2}}} \tag{2}$$

so that the effective traction takes the form of

$$\tau^{\mathrm{e}} = \boldsymbol{\tau} \cdot \mathbf{m}^{\mathrm{e}} = \bar{u}_0 (\boldsymbol{\tau} \cdot \mathbf{A}_{\mathrm{d}} \cdot \boldsymbol{\tau})^{\frac{1}{2}} \tag{3}$$

with the reference surface energy U_0 being the product of the reference decohesion scalar $\bar{u}_0$ and the corresponding traction $\bar{\tau}_0$. The components of the positive definite tensor of material parameters, $\mathbf{A}_{\mathrm{d}}$, with respect to the $\mathbf{n} - \mathbf{t}$ basis are given by

$$[\mathbf{A}_{\mathrm{d}}] = \bar{\tau}_0^2 \begin{bmatrix} \frac{1}{\tau_{\mathrm{nf}}^2} & 0 \\ 0 & \frac{1}{\tau_{\mathrm{tf}}^2} \end{bmatrix} \tag{4}$$

At the initiation of decohesion ($\lambda^{\mathrm{d}} = 0$), it follows from Eqs. (1.5), (3) and (4) that

$$\frac{\tau_{\mathrm{nb}}^2}{\tau_{\mathrm{nf}}^2} + \frac{\tau_{\mathrm{tb}}^2}{\tau_{\mathrm{tf}}^2} = 1 \tag{5}$$

where the normal and tangential tractions, τ_{nb} and τ_{tb} are obtained from the discontinuous bifurcation analysis. By letting $C_{\mathrm{m}} = \tau_{\mathrm{tf}}/\tau_{\mathrm{nf}}$ in Eq. (5), different failure modes can be simulated by utilizing different values of C_{m}. For example, mode I failure dominates if $C_{\mathrm{m}} = 10$, while mode II failure dominates if $C_{\mathrm{m}} = 0.1$. Mixed failure mode could be simulated by using $C_{\mathrm{m}} = 1$. Well-designed experiments are required to calibrate the value of C_{m}. The reference traction values, τ_{nf} and τ_{tf}, can be found from Eq. (5) evaluated at the initiation of bifurcation for given C_{m}. As can be seen from the above formulations, the discrete model parameters to be determined from the experiments are U_0, q and C_{m} if the choice of $\bar{\tau}_0 = \tau_{\mathrm{nf}}$ is made. Thus, the decohesion model could be calibrated via mode I experiments. The relation between the traction and decohesion can be adjusted by changing the value of q, as illustrated in Fig. 4.

3. MD simulation of single crystal W block under tension

In order to calibrate the parameters in the bifurcation-based decohesion model and develop a multi-scale decohesion–traction relation for W at different size scales, MD simulation of single crystal W block under

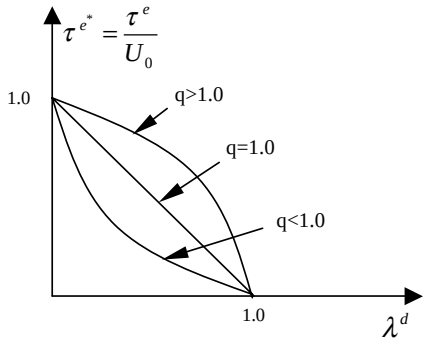

Fig. 4. Relationship between normalized effective traction and effective decohesion.

tension is conducted in this section. To be specific, the deformation fields and stress–strain curves of single crystal W blocks with different sizes are investigated under different tensile loading rates via MD.

3.1. Simulation procedure

The computational set-up for MD simulation of single crystal W block under uniaxial tension is shown in Fig. 5. The simulation super-cell is a three-dimensional box where x, y and z are the global coordinates. The simulation cell consists of two parts. One part is referred to as the active zone in which the atoms move according to the interactions among the neighboring atoms; the other part, wrapped by the boxes as shown in Fig. 5, is referred to as the boundary zone, where the atoms are assigned a constant velocity with a same magnitude but an opposite direction for each end, to simulate a displacement-controlled tensile loading in the z-direction. The dimension of the active zone is indicated by H, D and W, while the thickness of each boundary zone in the z-direction is $2a_o$ with a_o being the lattice parameter of W. A periodic boundary condition (PBC) is imposed along the x-direction. Either a PBC or a free surface (FS) will be applied in the y-direction.

Many studies (Milstein and Chantasiriwan, 1998; Roundy et al., 2001; Sob et al., 1998) have identified the $\langle 100 \rangle$ axes as the weak directions in tension and the $\{100\}$ planes as the cleavage planes for bcc tungsten. The crystal orientation of $(x[100], y[010], z[001])$ will therefore be investigated in this study since the decohesion process of single crystal W is of the interest in the current research. By simulating the separation of $\{100\}$ planes along the $\langle 100 \rangle$ direction via MD, a multi-scale decohesion model could be formulated as discussed later.

In the MD simulation, initially all atoms are placed at their equilibrium positions at room temperature of 298 K. Those atoms in the boundary zone are then fixed. After the system has equilibrated for a certain period, constant velocities with the same magnitude and opposite direction are assigned to the atoms in the top and bottom boundary zones, respectively, to simulate a displacement-controlled uniaxial tensile loading in the z-direction. A velocity scaling technique (Allen and Tildesley, 1990) is employed through the simulation to maintain a constant temperature of 298 K. The Embedded Atom Method (EAM) developed by Daw and Baskes (1984) is used to model the interatomic potential among W atoms. The method applied to integrate the equations of motion is the 6-value Gear predictor–corrector algorithm with corrector coefficients for a second-order equation. The integration time step size is determined based on the compromise between simulation accuracy and efficiency. The largest time step size that can keep the total system energy remaining a constant in the adiabatic simulations for W atoms with the EAM potential is used for the numerical study. To make the time integration stable, a time step size of 0.5 fs is chosen after several adiabatic simulations for W at different initial temperatures up to 2000 K.

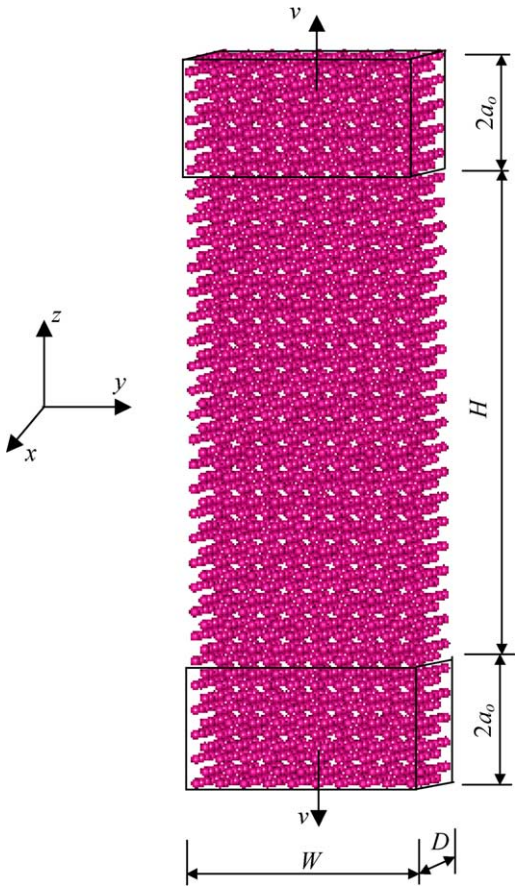

Fig. 5. A single crystal W block under uniaxial tensile load.

3.2. Embedded-atom method

The EAM developed by Daw and Baskes (1984) is a powerful tool to model the interatomic potential for metals and alloys. The basic equations of the EAM are given by

$$E = \sum_{ij,j>i} \phi(r_{ij}) + \sum_{i} F(\rho_i) \tag{6}$$

with

$$\rho_i = \sum_{j \neq i} f(r_{ij}) \tag{7}$$

where E is the total potential energy of the system, ρ_i is the electron density at atom i due to all other atoms, $f(r_{ij})$ is the electron density at atom i due to atom j as a function of the distance between them, r_{ij} is the separation distance between atoms i and j, $F(\rho_i)$ is the energy to embed atom i in an electron density ρ_i, and $\phi(r_{ij})$ is a two-body potential between atoms i and j. The detailed discussion on functions $\phi(r_{ij})$, $f(r_{ij})$ and $F(\rho_i)$ and the corresponding parameters for W can be found in the paper by Zhang and Ouyang (1993).

3.3. The calculations of stress and strain

Stress calculation in MD simulations has been a focus of study for many years (Cheung and Yip, 1991; Cormier et al., 2001; Horstemeyer et al., 2001; Irving and Kirkwood, 1950; Lovett and Baus, 1997; Wajnryb et al., 1995; Zhou, 2003). For the stress at a given atom, one could set up a volume element surrounding the atom, and calculate the force across each face of the element. This is a so-called mechanical definition which is conceptually straightforward but computationally quite tedious. The virial stress, derived from the virial theorem of Clausius (1870) as a thermodynamics approach to the formulation of atomic-level stress, is widely used to calculate the system pressure (Rowlinson and Widom, 1982). Cheung and Yip (1991) showed that the virial stress is equivalent to the mechanical definition of stress for a homogeneous system, and that the equivalence can be demonstrated using the concept of volume average if inhomogeneities occur. However, the virial stress includes two parts, namely, the first part involves the mass and velocity of atoms, and the second part accounts for the interatomic forces. Zhou (2003) argued that the widely used virial stress in discrete particle systems is not a measure for mechanical force between particles but rather a stress-like measure for momentum change in space. He proved that interpretation of the virial stress as a measure for mechanical force violates balance of momentum and demonstrated that the interatomic force part alone is a valid stress measure and can be identified with the Cauchy stress. In this study, the formulations employed to calculate atomic-level stress are motivated by the above discussions, as described next.

At each atom, the local stress tensor, $\boldsymbol{\beta}$, is given by

$$\boldsymbol{\beta}_i = -\frac{1}{\Omega_i}\sum_{j>i}^{N^n}\mathbf{f}_{ij}\otimes\mathbf{r}_{ij} \tag{8}$$

where i refers to the atom considered and j refers to the neighboring atom, $\mathbf{r}_{ij}$ is the position vector between atoms i and j, N^{n} is the number of neighboring atoms surrounding atom i, Ω_i is the volume of atom i, and $\mathbf{f}_{ij}$ is the force vector on atom i due to atom j. The global continuum stress tensor is defined as a volume average, namely,

$$\boldsymbol{\sigma} = \frac{1}{N^*}\sum_{i}^{N^*}\boldsymbol{\beta}_i \tag{9}$$

in which N^* represents the total number of atoms in a representative volume of continuum.

To deal with large deformations, true strain, a nonlinear strain measure that is dependent upon the current length of the specimen, is used in this study and is given by

$$\varepsilon = \ln(L/L_{\mathrm{o}}) \tag{10}$$

with L_{o} and L being the original and deformed lengths of the specimen, respectively.

3.4. Simulation results

To study the effect of boundary condition, specimen size and strain rate on the dynamic responses of single crystal W block under tensile loading, nine MD simulation cases are designed. The details of the simulation design are listed in Table 1. In all the simulations, a periodic boundary condition is applied in the x-direction. The boundary condition in the y-direction for each case is given in Table 1. The crystal orientation is ($x[1\,0\,0], y[0\,1\,0], z[0\,0\,1]$).

3.4.1. The effect of boundary conditions

Simulations 1–3 are conducted to study the effect of boundary conditions on the tensile deformation of single crystal W block. Fig. 6 shows the corresponding stress–strain curves. Although the stress reaches its

Table 1
Description of the MD simulation design

Simulation no.	Specimen size $D \times W \times H$ (nm^3)	Number of active atoms	Boundary condition	Initial strain rate (s^{-1})
1	$1.59 \times 1.59 \times 4.78$	750	FS	2×10^9
2	$1.59 \times 1.59 \times 4.78$	750	PBC	2×10^9
3	$1.59 \times 3.18 \times 4.78$	1500	FS	2×10^9
4	$1.27 \times 1.27 \times 3.83$	384	PBC	2×10^9
5	$2.54 \times 2.54 \times 7.65$	3072	PBC	2×10^9
6	$3.19 \times 3.19 \times 9.56$	6000	PBC	2×10^9
7	$6.38 \times 6.38 \times 19.13$	48,000	PBC	2×10^9
8	$3.19 \times 3.19 \times 9.56$	6000	PBC	2×10^8
9	$3.19 \times 3.19 \times 9.56$	6000	PBC	2×10^{10}

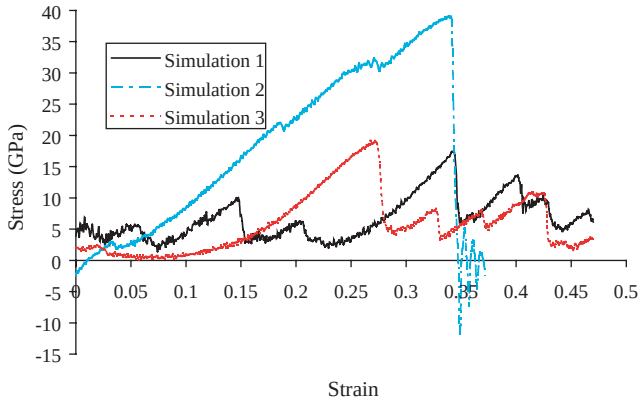

Fig. 6. The effect of boundary conditions on the stress–strain curve of W with crystal orientation of (x[100], y[010], z[001]) under initial strain rate of 2×10^9 s^{-1}.

peak value at about the strain of 0.34 in both Simulations 1 and 2, the peak stress with PBC in the y-direction is much larger than that with FS by using the same specimen size. In Simulation 2 the stress drops rapidly after its peak value and goes to zero at the strain of 0.348, however, the stress fluctuates for a very long strain range after the peak stress and does not reach zero even at the strain of 0.47 in Simulation 1. By doubling the specimen size in the y-direction in Simulation 3, the peak stress occurs at strain of 0.27, although its magnitude keeps almost the same as that of Simulation 1. The stress also fluctuates after its peak value and does not go to zero at the strain of 0.47. By comparing simulations 1 and 3, it appears that the strain corresponding to the peak stress is size-dependent with the FS boundary condition.

Fig. 7 presents the evolution of corresponding tensile deformation field in the y–z plane for Simulation 1. As can be seen from the figure, due to the use of FS and the lack of constraint in the y-direction the shrinking of the x–y cross sectional area in the active zone of Simulation 1 occurs when the stress reaches its peak value at the strain of 0.344. After the peak state, the stress fluctuates and the rearrangement of the crystal structure evolves as the strain increases. At the strain of 0.47, a severe necking occurs, but the corresponding stress is still not zero.

Fig. 8 shows the evolution of the corresponding tensile deformation field in the y–z plane for Simulation 2. The decohesion in Simulation 2, with the PBC in the y-direction, starts at the strain of 0.339 where the stress reaches its peak value, as shown in Fig. 8(a). The decohesion of W block evolves at the strain of 0.342, as shown in Fig. 8(b), and the complete separation of W block occurs at the strain of 0.345, as presented in Fig. 8(c). As a result, the cleavage of {100} planes is found at the end of decohesion in Simulation 2.

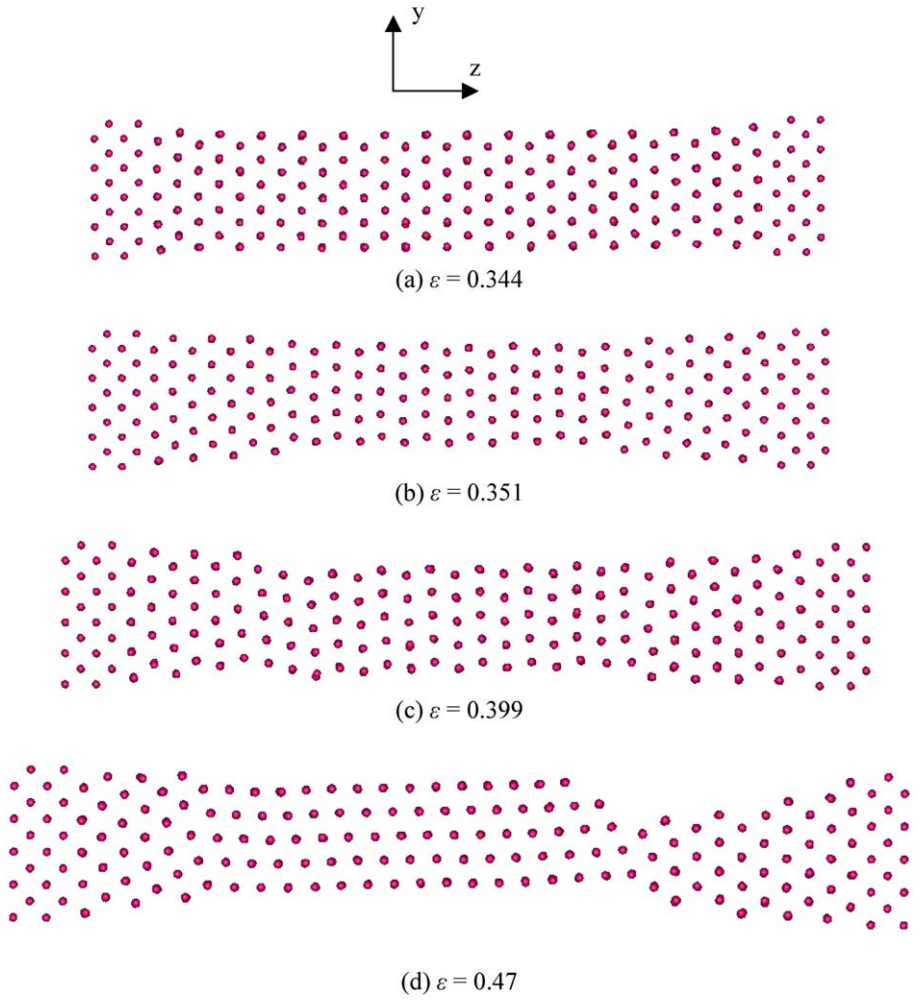

Fig. 7. The tensile deformation fields of Simulation 1 in the y–z plane at different strain levels.

It seems that neither decohesion nor cleavage of planes will occur with the use of FS in the y-direction since the cleavage of $\{100\}$ planes is avoided by the rearrangement of the crystal structure. Hence, in the following MD simulations a PBC is always applied in the both x- and y-directions in order to investigate the evolution of decohesion in single crystal W block under tensile loading, and to obtain the constitutive law of W at the nano-scale.

3.4.2. The effect of specimen size

To study the effect of specimen size on the tensile deformation of single crystal W, Simulations 2, 4–7 are performed with the PBC applied along both the x-and y-directions. Fig. 9 shows the corresponding stress–strain curves of different W blocks under tensile loading. As can be seen from the figure, the initial elastic modulus of single crystal W block is almost independent on the specimen size. However, the peak stress increases as the specimen size decreases, which is mainly due to the fact that larger specimens offer more opportunities for dislocation to occur. In addition to the constraints due to the boundary zones and the PBC used in the simulations, the single crystal W specimen is a discrete system with atoms distributed only

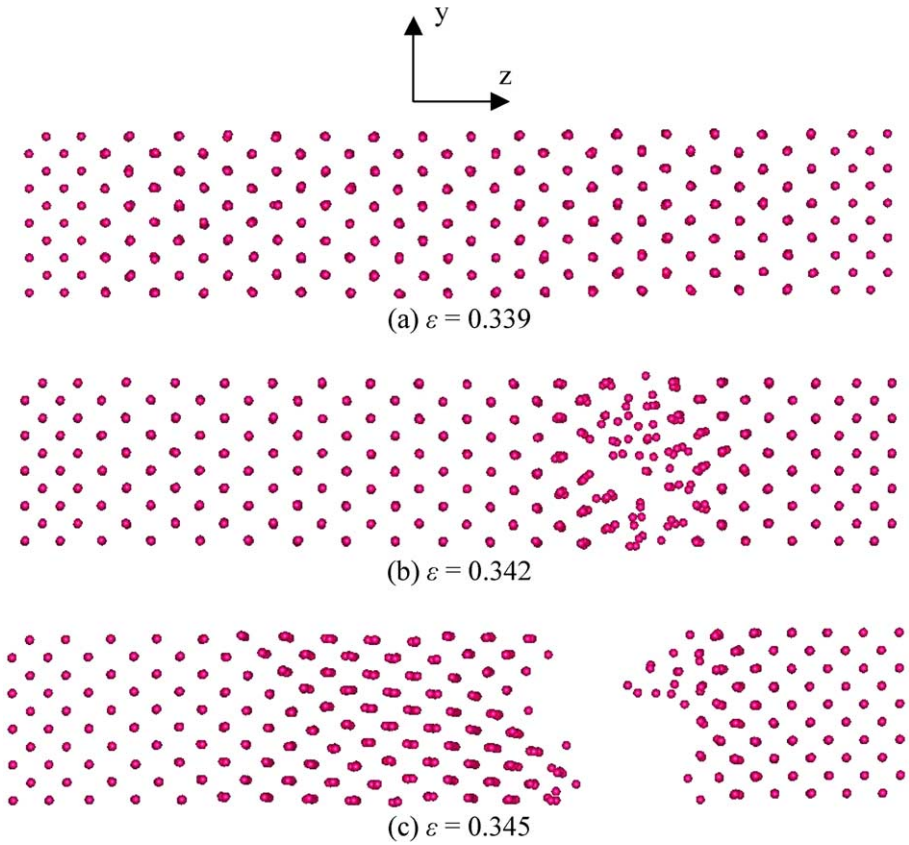

Fig. 8. The tensile deformation fields of Simulation 2 in the y–z plane at different strain levels.

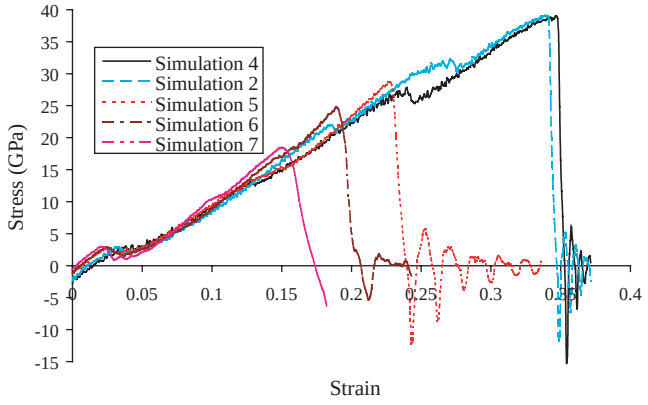

Fig. 9. The effect of W specimen size on the stress–strain curves with crystal orientation of (x[1 0 0], y[0 1 0], z[0 0 1]) under tensile strain rate of 2×10^9 s^{-1}.

in certain positions. The bonds among atoms are the relatively weak parts while the individual atoms are the strong parts of the system. The increase of specimen size increases the number of relatively weak bonds,

which in turn offers more opportunities for bond breaking and dislocation to occur, and thus decreases the strength of the specimen. However, the size effect is diminished as the specimen size is further increased as can be seen from Fig. 9.

3.4.3. The effect of defects

In the above simulations, the W specimens are perfect without any artificial imperfections. To verify the argument that the decrease of the W strength with the increase of specimen size is mainly due to the fact that a larger specimen offers more opportunities for dislocation to occur, the effect of artificially introduced defects in single crystal W block on the stress–strain relation is investigated. Different numbers of vacancies are artificially implemented into Simulation 2 with other simulation conditions being kept the same. The stress–strain curves of W blocks with zero, one, two and four vacancies distributed in the same x–y plane (which is initially located 2.152 nm away from the top end of the active zone) are demonstrated in Fig. 10. As can be seen from the figure, all stress–strain curves are initially the same until failure occurs. The strength of W decreases as the number of vacancies increases, since more vacancies offer more opportunities for bond breaking and dislocation to occur. However, the reduction rate of strength is decreasing with the increase of number of vacancies.

To study the effect of the vacancy distribution in the z-direction on the stress–strain relation of single crystal W block, four cases with zero, one, two and four vacancies, respectively, located at the center of x–y plane but different positions in the z-direction, are simulated with other simulation conditions being kept the same as those in Simulation 2. The corresponding stress–strain curves are presented in Fig. 11. As can be seen from the figure, all stress–strain curves are again initially the same until failure occurs, and the strength decreases as the number of vacancies increases, which is similar to the previous simulation with vacancies distributed in the same x–y plane. It seems that increasing the number of defects regardless of their positions in single crystal W block would increase the possibilities for dislocations to occur and thus reduce the strength of W, which is very similar to the effect of increasing specimen size on the strength of W. Therefore, it is reasonable to argue that larger specimens offer more opportunities for dislocations to occur which in turn reduces the strength of W.

3.4.4. The effect of machine precision

Since the artificially introduced defects would cause the decrease of the simulated W strength, it is therefore important to investigate the effect of machine precision on the simulation results. In the previous simulations, the default setting, i.e., double precision, is used for all the variables defined as real numbers. To

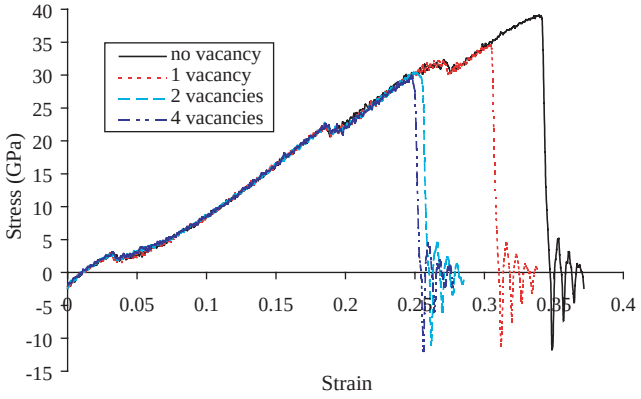

Fig. 10. Stress–strain curves of W blocks with different number of vacancies distributed in the same x–y plane.

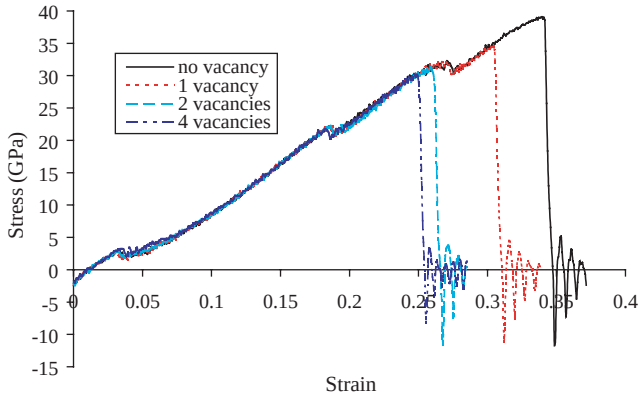

Fig. 11. Stress–strain curves of W with vacancies distributed along the same z-axis.

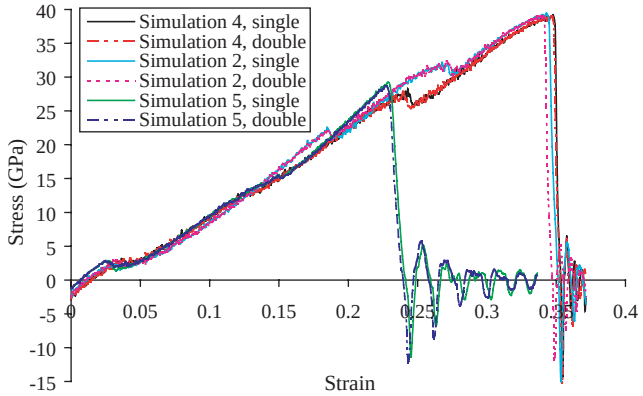

Fig. 12. The effect of machine precision on the stress–strain relation of single crystal W block under tensile loading.

study the effect of machine precision, Simulations 2, 4 and 5 are re-run by setting all the real variables to single precision with all other simulation conditions being kept the same. The MD program is written in *C*. All the simulations were run on an SGI workstation with Intel Pentium 4 processor and Linux operating system.

Fig. 12 illustrates the stress–strain curves of W blocks in Simulations 2, 4, and 5 by using single precision and double precision for all real variables in the program, respectively. As can be seen, there is no difference between the curves obtained by using single precision and those by using double precision before failure occurs, although failure occurs slightly later in the single precision case than does in the corresponding double precision case. Hence, the imperfection caused by machine precision is very small and may be neglected as compared to other imperfections or defects in the system.

3.4.5. The effect of strain rate

It is well known that loading rate could considerably influence the material properties, such as strength, ductility, etc., at the continuum level. To investigate the effect of the tensile strain rate on the stress–strain curve of a single crystal W block at the atomic level, Simulations 6, 8 and 9 are performed with the initial strain rate of $2\times10^{9}\,s^{-1}$, $2\times10^{8}\,s^{-1}$ and $2\times10^{10}\,s^{-1}$, respectively. Fig. 13 shows the corresponding

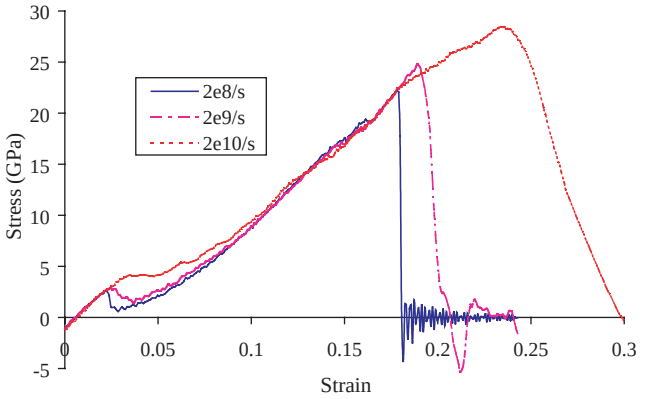

Fig. 13. The effect of strain rate on the stress–strain curve of single crystal W under tension.

stress–strain curves. As can be seen from the figure, the initial elastic modulus of W is almost independent on the strain rate, but the peak stress increases with the strain rate. The dependence of decohesion initiation on the strain rate is mainly due to the dynamic wave effect that impedes the motion of dislocations (Liang and Zhou, 2003).

4. Multi-scale decohesion–traction model for tungsten

In order to determine material properties for elasto-plasticity and decohesion at different scales, a power scaling law is proposed. In the proposed approach, the dependence of the strength and decohesion energy of W on the spatial size is established by combining the MD simulation of single crystal W block under tension and the available experimental data.

Power scaling in absence of characteristic length has been used to identify the material properties at different scales. By considering geometrically similar systems, the power scaling law takes the general form of (Bazant, 2002):

$$f(\lambda) = \lambda^m \tag{11}$$

where $\lambda = D_1/D_2$ with D_1 and D_2 being the characteristic sizes of two similar structures, respectively, $f(\lambda) = Y_1/Y_2$ is a dimensionless function with Y_1 and Y_2 being the material properties at sizes D_1 and D_2, respectively, and exponent m is an unknown constant.

To determine exponent m, a suitable failure criterion must be chosen. For elasto-plasticity with a fixed yield surface which is expressed only in terms of stress or strain, one finds that $m = 0$ when the material property Y represents the stress or strain. This is known as the case of no size effect on material strength, which is however only true when the size of the structure is within certain range. Indentation tests on single crystal W (Hutchinson, 2000) have shown that there is certain dependence of material hardness on crystal orientation, but the size-dependence is the predominant effect. However, indents on W with diagonals longer than about 100 μm cease to display any hardness-dependence on the size. Since the material hardness is directly related to the strength, the effect of structure size on the material strength exists when the structure size is smaller than about 100 μm, namely, $m \neq 0$ when $D < 100$ μm. No size effect would occur as the structure size is beyond about 100 μm, namely, $m = 0$ when $D \geqslant 100$ μm. It seems that the exponent m will change from nonzero to zero when the structure reaches the critical size of about 100 μm.

Since there is an effect of strain rate on the strength of crystal W when the strain rate is high, a factor is needed to approximately account for the influence of the strain rate. MD simulations of sheared single

crystal metals conducted by Horstemeyer et al. (2001) have demonstrated some qualitative features: (a) strain rate independence at low strain rate, and (b) an increase in the critical strain rate, under which rate-dependence disappears, with a decrease of specimen size. Their simulation results have shown that there is no strain rate effect on nickel's yield strength with specimen size smaller than 28 nm when the strain rate is in the order of $10^8\ s^{-1}$. It is therefore assumed in this study that the strength of W obtained with the strain rate of $2\times10^8\ s^{-1}$ is rate-insensitive since the specimen sizes are smaller than 28 nm. As can be seen from Fig. 13, the strength of W in Simulation 6, decreases from 24.8 GPa at the rate of $2\times10^9\ s^{-1}$ to 22.2 GPa at the rate of $2\times10^8\ s^{-1}$ in Simulation 8 with a factor of $22.2/24.8 = 0.895$. For the sake of simplicity, all the strengths obtained in Simulations 2, 4–7 with the strain rate of $2\times10^9\ s^{-1}$, as shown in Fig. 9, will be multiplied by a factor of 0.895 to approximately calculate the rate-independent strengths at different structure sizes under strain rates in the order of $10^8\ s^{-1}$.

By combining the MD simulation data and the available experimental results, a multi-scale strength model for W is proposed here based on the assumption that the exponent m in the power scaling law must change smoothly when the structure size increases from atomic-scale to macro-scale. Fig. 14 presents the MD simulation data for the rate-independent strength of a single crystal W block at different structural sizes, the strength of W at the macro-scale from experiments, and the proposed multi-scale model prediction of W strength. The model proposed to predict the multi-scale strength of W takes the form of

$$\begin{cases} \sigma_N = \sigma_P & D \leqslant D_P \\ \dfrac{\lg\sigma_N - \lg\sigma_M}{\lg\sigma_P - \lg\sigma_M} = 1 - \sin\left[\dfrac{\pi}{2}\times\dfrac{\lg D - \lg D_P}{\lg D_M - \lg D_P}\right] & D_P < D < D_M \\ \sigma_N = \sigma_M & D \geqslant D_M \end{cases} \tag{12}$$

where D is the characteristic size of W specimen, D_P is the maximum atomic-scale size of W specimen at which the ultimate tensile strength of W is reached, D_M is the minimum macro-scale size of W specimen where the tensile strength of W ceases its dependence on the size, σ_N is the nominal strength of W at size D, σ_M is the strength of W at size D_M, and σ_P is the ultimate tensile strength of W. Based on the MD simulations of single crystal W block under tensile loading, $\sigma_P = 34.9$ GPa at $D_P = 1.6$ nm, which is in a reasonable agreement with the maximum tensile strength of 29.5 GPa as reported by Roundy et al. (2001) using pseudopotential density functional theory, is applied. According to Hutchinson (2000), $D_M = 100\ \mu m$ is assumed. As a common material property for W, $\sigma_M = 1.5$ GPa is adopted in this study.

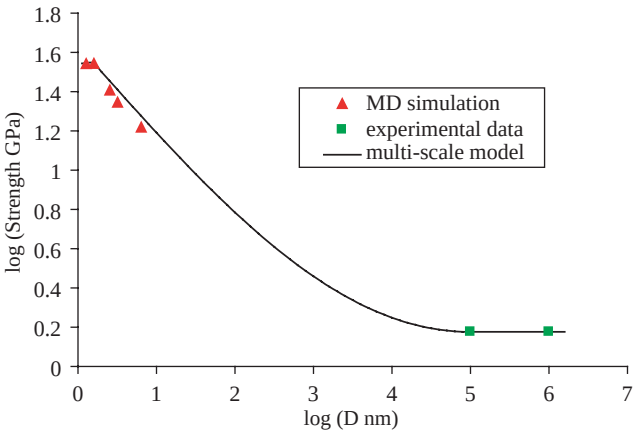

Fig. 14. Multi-scale model prediction of the strength of W at different sizes.

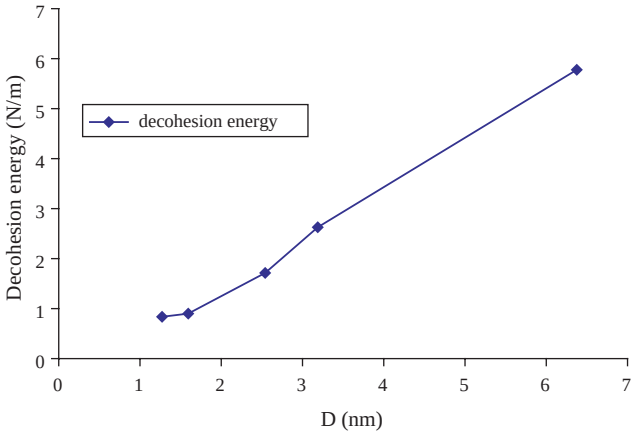

Fig. 15. The size effect on the decohesion energy of single crystal W block with crystal orientation of ($x[1\,0\,0], y[0\,1\,0], z[0\,0\,1]$) under tension.

Fig. 15 presents the effect of specimen size on the decohesion energy of single crystal W with crystal orientation of ($x[1\,0\,0], y[0\,1\,0], z[0\,0\,1]$) under tension. The decohesion energy can be estimated based on the area under the corresponding stress–strain curve within the softening regime in Fig. 9, with a factor of 0.895 being multiplied to approximately account for the rate effect on the strength. As can be seen from Fig. 8, the failure of the W block is an averaged process since the breaking of the bonds across the failure surfaces cannot occur at the same time. When the specimen size increases, more bonds need to be broken before the complete separation of the specimen can occur, which would extend the whole failure evolution process and thus increases the simulated decohesion energy. However, the size-dependence of decohesion energy would diminish as the specimen size is decreased. Hence, the simulated data based on a smaller specimen could provide a more accurate estimation of the decohesion energy of W. Thus, the decohesion energy of W is chosen to be 0.835 N/m based on Simulation 4, as shown in Fig. 15.

For the bifurcation-based decohesion model defined by Eq. (1), U_0, τ_{nf}, q and C_{m} are the only four model parameters to be determined. If the size-dependent strength of W is obtained by using Eq. (12), τ_{nf} can then be calculated based on Eq. (5) through bifurcation analysis for a given failure mode. Since the reference surface energy U_0 is defined as $\bar{u}_0\bar{\tau}_0$ instead of $0.5(\bar{u}_0\bar{\tau}_0)$, U_0 is chosen to be 1.67 N/m because the simulated decohesion energy of tungsten is 0.835 N/m. If a linear decohesion–traction relation, namely, $q = 1$ in Eq. (1), is assumed and C_{m} is determined through well-designed experiments, a multi-scale decohesion–traction model can then be established for W.

5. Multi-scale simulation of thin film delamination

Based on the proposed multi-scale simulation procedure, as shown in Fig. 1, a plane-strain problem for simulating the thin film delamination process is designed. The problem configuration is shown in Fig. 16. The demension of specimen is given as $L = 10$ μm, $h_t = 2.5$ μm and $h_s = 5$ μm, respectively. The strength of tungsten is $\sigma_p \cong 2.3$ GPa based on Eq. (12) by considering the effect of the film thickness. The corresponding yield strength of W is assumed to be $\sigma_y \cong 1.53$ GPa. Since the elastic modulus is size-independent, $E = 411$ GPa is employed with Poisson's ratio $\nu = 0.28$ and mass density $\rho = 15{,}000$ kg/m^3. Before the discontinuous bifurcation occurs, the associated von Mises elasto-plasticity model with a linear hardening/softening function is used for W. After bifurcation occurs, the discrete constitutive model is active with

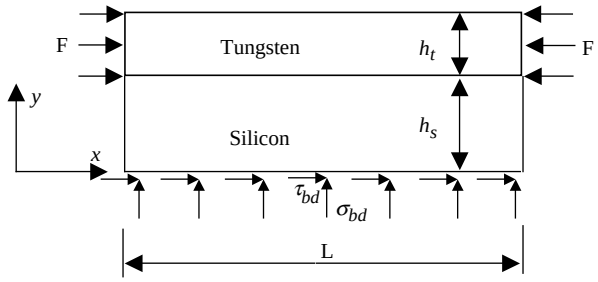

Fig. 16. Geometry and boundary conditions for a plane strain problem.

$U_0 = 1.67$ N/m, $q = 1.0$, and $C_m = 1.0$, 10.0 and 0.1 for mixed mode, mode I and mode II failures, respectively. Since the yield strength of Si is much higher than the strength of W, decohesion is not active inside Si and no size effect is thus considered for Si. An elasto-perfectly-plastic von Mises model is employed for Si, with Young's modulus $E = 107$ GPa, Poisson's ratio $v = 0.42$, mass density $\rho = 3200$ kg/m^3, and yield strength $\sigma_y = 8.0$ GPa. A step compressive stress of 1.8 GPa is uniformly applied along both ends of tungsten film at the time $t = 0$ to simulate the dynamic failure response.

Note that the designed substrate thickness is chosen to be much smaller than that in the real film–substrate problem in order to save computational costs. To reduce the effect of stress wave reflection from the bottom boundary of the substrate on the film failure pattern, a silent boundary is applied along the bottom surface of the substrate (Shen and Chen, in press). The MPM is used to discretize the film–substrate problem. The computational grid consists of square cells with each side being 1×10^{-7} m long. Initially, one material point per cell is used to discretize both tungsten and silicon. As a result, the interfacial strength would be the average of tungsten and silicon strengths due to the inherent nature of the mapping procedure in the MPM (Chen et al., 2002). To observe the deformation patterns clearly, the deformation fields are magnified by 10 times in both the x- and y-directions.

The effect of failure modes on the deformation pattern of the film–substrate structure is investigated by setting $C_m = 10.0$, 0.1 and 1.0, respectively, in the decohesion model for W film. Figs. 17–19 present the failure patterns of the W–Si structure at the time $t = 2.88$ μs with mode I failure, at the time $t = 1.92$ μs

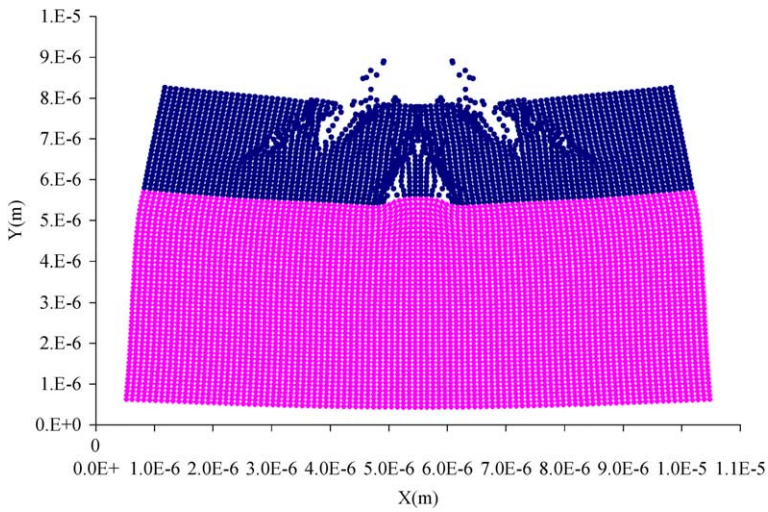

Fig. 17. Failure pattern of film–substrate structure at $t = 2.88$ μs with mode I failure.

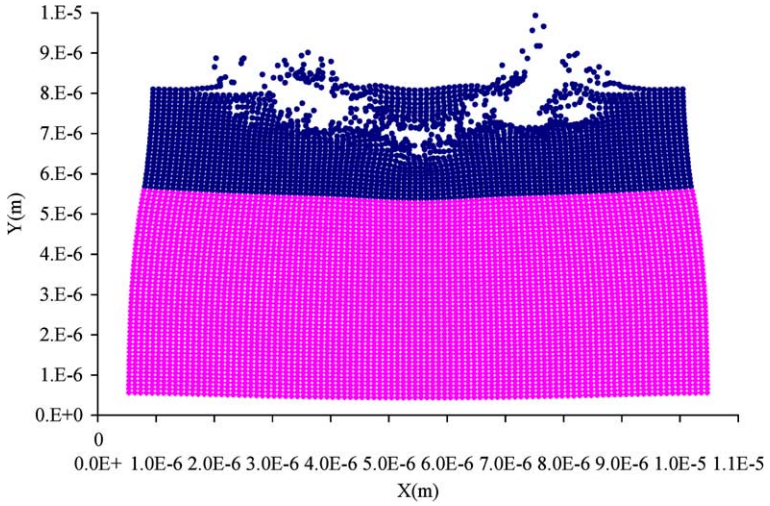

Fig. 18. Failure pattern of film–substrate structure at $t = 1.92$ μs with mode II failure.

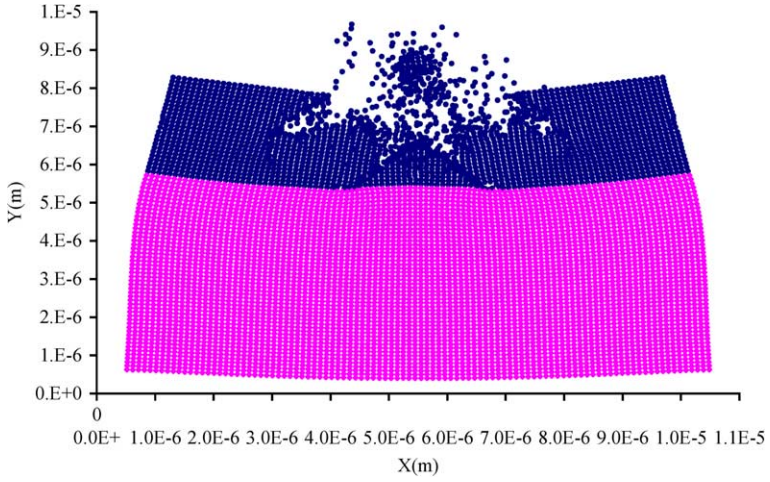

Fig. 19. Failure pattern of film–substrate structure at $t = 2.88$ μs with mixed mode failure.

with mode II failure, and at the time $t = 2.88$ s with mixed mode failure, respectively. Since the film will be severely damaged at the time $t = 2.88$ μs with mode II failure, only the deformation field of film–substrate structure at $t = 1.92$ μs is shown for mode II failure. As can be seen from Figs. 17 and 19, the decohesion might initiate at the top film surface and evolve deeply into the film until reaching the film–substrate interface with mode I and mixed model failures. However, the complete delamination of the film might occur before the film decohesion reaches the film–substrate interface with mode II failure, as shown in Fig. 18. It appears that the decohesion evolves quicker and the damage is severer if mode II failure is dominant as compared with mode I and mixed mode failures. This might be due to the fact that the von Mises model predicts mode II failure that governs the initiation and evolution of decohesion after the discontinuous bifurcation is identified. Note that the use of a silent boundary along the bottom surface of the Si substrate effectively removes the stress wave reflection from the otherwise fixed boundary, and provides a better simulation of the film delamination process.

6. Conclusions

In this paper, a multi-scale model-based simulation procedure for the film delamination process is proposed via a sequential approach. In the proposed procedure, a bifurcation-based decohesion model is first formulated within the framework of the MPM. A multi-scale decohesion–traction model for W is then established by using MD simulation of single crystal W block under tensile loading and available experimental data with a power scaling law to account for the size effect. The application to the model-based simulation of W film delamination from Si substrate demonstrates the potential of the proposed multi-scale simulation procedure.

To calibrate the parameters of the bifurcation-based decohesion model, MD simulation of W block with crystal orientation of ($x[1\,0\,0], y[0\,1\,0], z[0\,0\,1]$) under tension is conducted by using the EAM potential. The effects of boundary condition, specimen size, number of vacancies, machine precision and strain rate on the stress–strain relation curves are investigated at the atomic level. It is found that shrinking of specimen cross sectional area and rearrangement of crystal structure will occur with the FS boundary being applied in either direction, while the evolution of the decohesion and the subsequent separation of W specimen would occur with the use of PBC in both the x- and y-directions. Investigations of the size effect on material properties for W demonstrate that the initial elastic modulus of W is insensitive to the specimen size. However, the peak stress increases as the specimen size decreases, which is mainly due to the fact that larger specimens offer more opportunities for dislocation to occur. The argument is further verified by MD simulation of single crystal W block with artificially introduced vacancies under tension, since the increase of vacancies in W block reduces the strength of W regardless of the distribution of the defects. It is also shown that the influence of machine precision on the stress–strain curve of W obtained from MD simulation is not significant as compared to other factors, and might therefore be neglected. The initial elastic modulus of W is rate-insensitive, while the peak stress increases with the strain rate.

A multi-scale model for predicting W strength from atomic to continuum scales is formulated with the use of power scaling law. The model parameters are calibrated by combining the MD simulations of single crystal W block under tension and the macro-scale experimental results for W. By combining the multi-scale strength model and the decohesion energy obtained through the MD simulation, a multi-scale decohesion–traction model for W is developed. Simulation of W film delaminating from Si substrate with the proposed multi-scale decohesion model demonstrates that the decohesion evolves quicker and the damage is severer if mode II failure is dominant as compared with mode I failure and mixed mode failure. As can be seen from Figs. 17–19, blistering might also initiate at discrete nucleation sites, although it usually initiates in the neighborhood of the film's edge and propagates towards the center of the specimen.

Since the size effect on the strength of W film is considered and the decohesion energy is obtained via MD simulation, the multi-scale simulation of W film delamination from Si substrate could provide a better insight into the mechanisms of the film delamination process. However, the proposed multi-scale model for predicting W strength at different structural sizes is based on the MD simulation at the nano-scale and the experimental data for W at the macro-scale. Hence, an integrated experimental, analytical and numerical investigation on the structures with sizes ranging from nano to macroscales is required to verify the proposed multi-scale simulation procedure. Especially, well-designed experiments are needed to quantitatively explore the film delamination mechanisms at different scales.

Acknowledgements

This work was sponsored in part by the NSF-NIRT program under Grant No. 0304472, and by the Overseas Young Investigator Award from the Natural Science Foundation in China (NSFC Grant No. 10228206). The authors are grateful to the NIRT members: Profs. Espinosa, Hersam, Belytschko and

Schatz at Northwestern University, and Prof. Auciello at the University of Illinois at Chicago, as well as the collaborators at Argonne National Laboratory, Drs. Carlisle and Zapol, for joint discussions. The authors are also grateful to the reviewers for their discerning comments on this paper.

References

Allen, M.P., Tildesley, D.J., 1990. Computer Simulation of Liquids. Oxford University Press, p. 231.

Audoly, B., 1999. Stability of straight delamination blisters. Physics Review Letters 83, 4124–4127.

Bazant, Z.P., 2002. Scaling of Structural Strength. Taylor and Francis.

Chen, Z., Fang, H.E., 2001. A study on the link between coupled plasticity/damage and decohesion for multi-scale modeling. Journal of Mechanical Engineering Science—Proceedings of the Institution of Mechanical Engineers Part C 215, 259–263.

Chen, Z., Hu, W., Shen, L., Xin, X., Brannon, R., 2002. An evaluation of the MPM for simulating dynamic failure with damage diffusion. Engineering Fracture Mechanics 69, 1873–1890.

Chen, Z., Shen, L., Mai, Y.-W., Shen, Y.G., in press. A bifurcation-based decohesion model for simulating the transition from localization to decohesion with the MPM. Journal of Applied Mathematics and Physics (ZAMP).

Cheung, K.S., Yip, S., 1991. Atomic-level stress in an inhomogeneous system. Journal of Applied Physics 70, 5688–5690.

Clausius, R., 1870. On a mechanical theory applicable to heat. Philosophical Magazine 40, 122–127.

Cormier, J., Rickman, J.M., Delph, T.J., 2001. Stress calculation in atomistic simulations of perfect and imperfect solids. Journal of Applied Physics 89, 99–104.

Crosby, K.M., Bradley, R.M., 1999. Pattern formation during delamination and buckling of thin films. Physical Review E 59, R2542–R2545.

Daw, M.S., Baskes, M.I., 1984. Embedded-atom method: Derivation and application to impurities, surfaces, and other defects in metals. Physical Review Letter 29, 6443–6453.

Gioia, G., Ortiz, M., 1997. Delamination of compressed thin films. Advances in Applied Mechanics 33, 119–192.

Horstemeyer, M.F., Baskes, M.I., Plimpton, S.J., 2001. Computational nanoscale plasticity simulations using embedded atom potentials. Theoretical and Applied Fracture Mechanics 37, 49–98.

Hu, S.Y., Ludwig, M., Kizler, P., Schmauder, S., 1998. Atomistic simulations of deformation and fracture of α-Fe. Modelling and Simulation in Materials Science and Engineering 6, 567–586.

Huang, R., Suo, Z., 2002. Wrinkling of a compressed elastic film on a viscous layer. Journal of Applied Physics 91 (3), 1135–1142.

Hutchinson, J.W., Suo, Z., 1991. Mixed mode cracking in layered materials. Advances in Applied Mechanics 29, 63–191.

Hutchinson, J.W., 2000. Plasticity at the micron scale. International Journal of Solids and Structures 37, 225–238.

Irving, J.H., Kirkwood, J.G., 1950. The statistical mechanical theory of transport process IV the equations of hydrodynamics. Journal of Chemical Physics 18, 817.

Klein, P.A., Foulk, J.W., Chen, E.P., Wimmer, S.A., Gao, H., 2000. Physics-based modeling of brittle fracture: Cohesive formulations and the application of meshfree methods. SAND2001-8099, Sandia National Laboratories, USA.

Li, J., Yip, S., 2002. Atomistic measures of materials strength. Computer Modeling in Engineering and Sciences 3, 219–227.

Liang, W., Zhou, M., 2003. Size and strain rate in tensile deformation of Cu nanowires. Nanotech 2, 452–455.

Lovett, R., Baus, M., 1997. A molecular theory of the Laplace relation and of the local forces in a curved interface. Journal of Chemical Physics 106, 635–644.

Makarov, P.V., Schmauder, S., Cherepanov, O.I., Smolin, I.Y., Romanova, V.A., Balokhonov, R.R., Saraev, D.Y., Soppa, E., Kizler, P., Fischer, G., Hu, S., Ludwig, M., 2001. Simulation of elastic–plastic deformation and fracture of materials at micro- and macrolevels. Theoretical and Applied Fracture Mechanics 37, 183–244.

Milstein, F., Chantasiriwan, S., 1998. Theoretical study of the response of 12 cubic metals to uniaxial loading. Physical Review B 58, 6006–6018.

Moldovan, D., Golubovic, L., 1999. Tethered membranes far from equilibrium: Buckling dynamics. Physical Review E 60, 4377–4384.

Roundy, D., Krenn, C.R., Cohen, M.L., Morris, J.W., 2001. Ideal strength of BCC tungsten. Philosophical Magazine A 81, 1725–1747.

Rowlinson, J.S., Widom, B., 1982. Molecular Theory of Capillarity. Clarendon, Oxford, p. 85.

Schreyer, H.L., Sulsky, D.L, Zhou, S.-J., 1999. Modeling material failure as a strong discontinuity with the material point method. In: Pijaudier-Cabot, G. (Ed.), Mechanics of Quasi-brittle Materials and Structures: A Volume in Honor of Professor Zdenek P. Bazant's 60th Birthday. Hermes Science Publications, Paris, pp. 307–329.

Shen, L., Chen, Z., in press. A silent boundary scheme with the material point method for dynamic analyses. Computer Modeling in Engineering and Sciences.

Shen, Y.G., Mai, Y.-W., Zhang, Q.C., McKenzie, D.R., Fall, W.D., McBride, W.E., 2000. Residual stress, microstructure, and structure of tungsten thin films deposited by magnetron sputtering. Journal of Applied Physics 87, 177–187.

Sob, M., Wang, L.G., Vitek, V., 1998. The role of higher-symmetry phases in anisotropy of theoretical tensile strength of metals and intermetallics. Philosophical Magazine B 78, 653–658.

Wajnryb, E., Altenberger, A.R., Dahler, J.S., 1995. Uniqueness of the microscopic stress tensor. Journal of Chemical Physics 103, 9782–9787.

Wan, K.T., Mai, Y.-W., 1995. Fracture-mechanics of a New Blister Test with stable crack-growth. Acta Metallurgica et Materialia 43, 4109–4115.

Xu, X.P., Needleman, A., 1994. Numerical simulations of fast crack growth in brittle solids. Journal of the Mechanics and Physics of Solids 42, 1397–1434.

Zhang, B., Ouyang, Y., 1993. Theoretical calculation of thermodynamics data for BCC binary alloys with the embedded-atom method. Physical Review B 48, 3022–3029.

Zhou, M., 2003. A new look at the atomic level virial stress: on continuum-molecular system equivalence. Proceedings of the Royal Society of London A 459, 2347–2392.